Available online at www.sciencedirect.com
SCIENCE DIRECT®
Journal of Structural Biology 147 (2004) 235–246
Journal of Structural Biology
www.elsevier.com/locate/yjsbi

Picosecond time-resolved X-ray crystallography: probing protein function in real time

Friedrich Schotte[a], Jayashree Soman[b], John S. Olson[b], Michael Wulff[c], Philip A. Anfinrud[a,*]

[a] *Laboratory of Chemical Physics, NIDDK, National Institutes of Health, Bethesda, MD 20892, USA*
[b] *Department of Biochemistry and Cell Biology, The W. M. Keck Center for Computational Biology, Rice University, Houston, Texas 77251-1892, USA*
[c] *Experiments Division, European Synchrotron Radiation Facility, 38000 Grenoble, France*

Received 27 March 2004, and in revised form 17 June 2004

Abstract

A detailed mechanistic understanding of how a protein functions requires knowledge not only of its static structure, but also how its conformation evolves as it executes its function. The recent development of picosecond time-resolved X-ray crystallography has allowed us to visualize in real time and with atomic detail the conformational evolution of a protein. Here, we report the photolysis-induced structural evolution of wild-type and L29F myoglobin over times ranging from 100 ps to 3 μs. The sub-ns structural rearrangements that accompany ligand dissociation in wild-type and the mutant form differ dramatically, and lead to vastly different ligand migration dynamics. The correlated protein displacements provide a structural explanation for the kinetic differences. Our observation of functionally important protein motion on the sub-ns time scale was made possible by the 150-ps time resolution of the measurement, and demonstrates that picosecond dynamics are relevant to protein function. To visualize subtle structural changes without modeling, we developed a novel method for rendering time-resolved electron density that depicts motion as a color gradient across the atom or group of atoms that move. A sequence of these time-resolved images have been stitched together into a movie, which allows one to literally "watch" the protein as it executes its function.
Published by Elsevier Inc.

Keywords: Myoglobin; Protein dynamics; Protein function; Time-resolved X-ray crystallography; Laue; Picosecond

1. Introduction

Since the pioneering work of Frauenfelder and co-workers (Austin et al., 1975), myoglobin (Mb) has served as a useful model system for probing the relations between protein structure, dynamics, and function. Myoglobin is a heme protein (Fig. 1A) found in muscle that reversibly binds O_2 as well as other physiological ligands such as CO and NO. The photosensitive Fe—ligand bond has allowed transient intermediates to be studied by numerous flash photolysis methods and has made myoglobin one of the most thoroughly studied proteins. Of the three adducts, MbCO is most stable and most easily photolyzed (Gibson and Ainsworth, 1957; Olson and Phillips, 1996; Ye et al., 2002), and has been the target of most time-resolved studies. For example, time-resolved IR investigations of photolyzed MbCO showed that CO becomes temporarily trapped in a nearby ligand docking site before escaping into the surrounding solvent (Lim et al., 1995). Molecular dynamics (MD) simulations suggested a location for this docking site (Carlson et al., 1994; Gibson et al., 1992; Quillin et al., 1995; Sassaroli and Rousseau, 1986; Vitkup et al., 1997), which was found to be consistent

* Corresponding author. Fax: +301-435-6710.
E-mail address: anfinrud@nih.gov (P.A. Anfinrud).

1047-8477/$ - see front matter. Published by Elsevier Inc.
doi:10.1016/j.jsb.2004.06.009

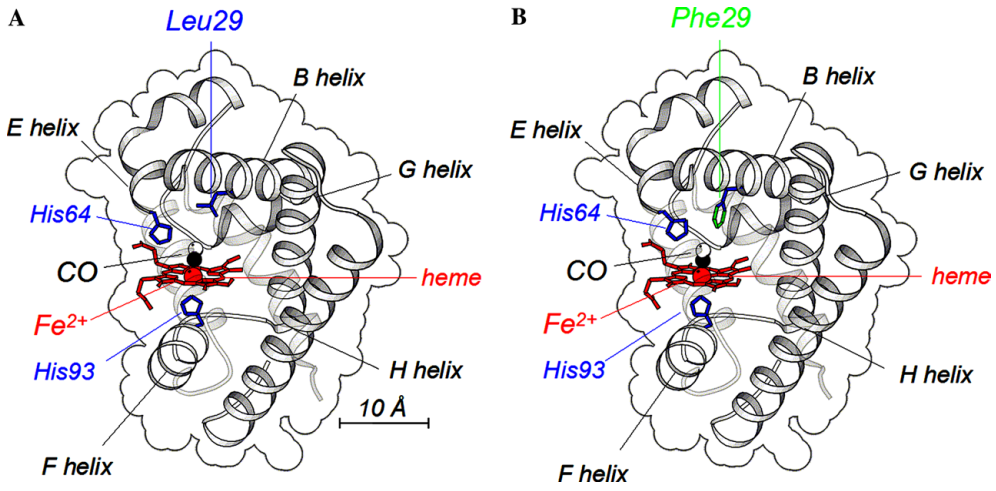

Fig. 1. Structure of wild-type (A) and L29F (B) MbCO. The heme and several key residues are modeled as sticks, the iron and CO as space filling spheres, and the protein as ribbon with its space-filling volume outlined. In the L29F mutant of Mb, leucine (L; blue) in the 29 position is replaced by phenylalanine (F; green).

with low-temperature crystal structures of photolyzed MbCO (Schlichting et al., 1994; Teng et al., 1994) where "docked" CO was displaced about 2 Å from the active binding site. This docking site, which presumably mediates the transport of ligands to and from the active binding site, is fashioned primarily by the heme and amino acid side chains Leu29, Val68, and Ile107 (Elber and Karplus, 1990), all of which are highly conserved in mammalian Mb. Apparently, nature has tuned the structure and conformational flexibility of these residues to optimize the reversible binding of O_2. Therefore, site-directed mutagenesis at these sites would likely influence the function of the protein. Indeed, an experimental and MD study of 29 position mutants illustrated how the packing of residues circumscribing the heme pocket influences the kinetics and pathways of ligand migration

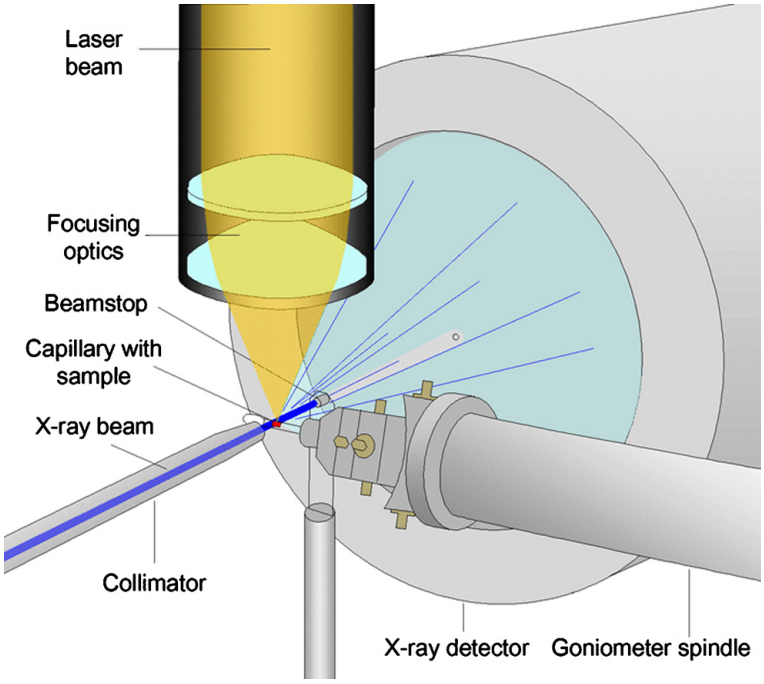

Fig. 2. Sample geometry used to acquire picosecond time-resolved X-ray diffraction data. The MbCO crystal was photolyzed by a 100-ps laser pulse and probed by a time-delayed 150-ps X-ray pulse, whose diffraction pattern was recorded on an X-ray sensitive area detector. The crystal ($0.24 \times 0.24 \times 0.7$ mm) was mounted in a sealed capillary filled with CO at 1-atm pressure. The laser pulse was guided to the sample by an optical fiber and focused to a 0.11×0.24 mm spot on the surface of the crystal. The X-ray beam of 0.05×0.12 mm (V/H) passed through the pump-illuminated volume of the crystal.

(Gibson et al., 1992). Of particular interest is the functional effects of the L29F mutation (Fig. 1B), where Leu29 (L) is replaced by phenylalanine (F): its O_2 affinity is elevated by an order of magnitude and its autooxidation rate is lowered by a comparable amount (Carver et al., 1992). As we show in this paper, time-resolved structures unveil the mechanistic origins of some of the functional differences between wild-type and L29F Mb.

To gain mechanistic insights into the function of a protein, it is crucial to know how its structure evolves in time as it executes its designed function. Time-resolved spectroscopic methods are well suited to probe the dynamics of various processes on time scales down to femtoseconds; however, the structural details, including the direction, amplitude, and timescale of functionally important protein motions are usually left to one's imagination. Molecular dynamics simulations (Brooks et al., 1988; McCammon and Harvey, 1987) help guide our imagination, but the time range accessible to a statistically compelling set of all-atom simulations is currently limited to the nanosecond time regime, and without experimental validation of the potentials used in the simulations, one may question the predictions. Cryo-crystallography has emerged as a powerful tool for characterizing the structure of intermediates that can be trapped at low temperatures (Brunori et al., 2000; Chu et al., 2000; Ostermann et al., 2000; Schlichting and Chu, 2000). The high-resolution capabilities of this method provide clues to the structural identity of putative intermediates along the reaction pathway, but their dynamics are not characterized, and functionally relevant protein motions may be frozen out at the low temperatures required by this method. To characterize structural evolution at ambient temperature, the method of time-resolved X-ray crystallography has been developed (Moffat, 2001). The pioneering efforts of Moffat and co-workers led to the first nanosecond time-resolved structure of a protein (Srajer et al., 1996), and subsequent studies improved the spatial resolution attained (Bourgeois et al., 2003; Brunori et al., 2004; Srajer et al., 2001). We recently developed the method of picosecond X-ray crystallography and used this technique to structurally characterize the L29F mutant of myoglobin as it evolves from the carboxy to the deoxy state (Schotte et al., 2003). Whereas the spatial resolution of this technique is not as high as that achieved using cryo-crystallography, the ability to follow structural changes on a time scale accessible to MD simulations is crucial to our efforts to understand how proteins function in atomic detail. Here, we report time-resolved structures of wild-type MbCO and compare them with those from L29F MbCO. To help make this comparison, we introduce a novel method for visualizing the structural changes.

2. Materials and methods

The experiments reported here were performed on the ID09B beamline at the European Synchrotron Radiation Facility (ESRF) in Grenoble, France. The data acquisition protocol used to acquire time-resolved structures of L29F MbCO was reported elsewhere (Schotte et al., 2003). The protocol used for wild-type MbCO is described in detail here. Briefly, a visible laser pulse photolyzed the protein crystal and a time-delayed X-ray pulse probed the protein structure through its diffraction pattern (see Fig. 2). Because binding of CO to myoglobin is reversible, the measurement could be repeated thousands of times as a function of crystal orientation and time delay. From the set of diffraction images collected, "snapshots" of the protein structure were determined at time delays ranging from 100 ps to 3 μs. These structures unveil ligand migration and correlated motion of the protein at a high level of detail.

2.1. Sample preparation

Sperm whale Mb was expressed from recombinant DNA in *Escherichia coli*. The wild-type and L29F forms of Mb have a methionine initiator and an asparagine (Asn) that replaces the aspartate (Asp) in the 122 position. The latter mutation causes the protein to crystallize in the spacegroup P6 ($a = b = 91.2$ Å, $c = 45.7$ Å, $\alpha = \beta = 90°$, and $\gamma = 120°$) (Phillips et al., 1990) rather than $P2_1$, the crystal form often adopted by native Mb. For simplicity, we refer to the Asp122Asn mutant as "wild-type," because this mutation is located on the surface of the protein and does not alter its physiological function. Because of its sixfold symmetry, a complete set of data requires only 60° of rotation, speeding up the Laue data collection.

Crystals of sperm whale myoglobin were grown from seeds implanted in hanging drops. Upon reaching maturity, they were transferred to vials and stabilized in 3.2 M ammonium sulfate, pH 9.0. Selected crystals were reduced with sodium dithionite and sealed in X-ray capillaries under a CO atmosphere with mineral oil plugs deposited on either side. The mineral oil minimized cooling/heating-driven distillation of mother liquor to/from the crystal when placed under a cooling stream and illuminated by the pump laser.

2.2. Laser source

Broadly tunable photolysis pulses of ~100 fs duration were produced by an optical parametric amplifier (OPA: Quantronix, TOPAS) that was pumped by the output (800 nm, ~100 fs, 1 mJ) from a Ti:sapphire regenerative amplifier (Spectra Physics, Hurricane). Because the seed laser inside the Hurricane cannot be synchronized to an external frequency, it was purchased without the inter-

nal laser and was externally seeded with pulses generated in a femtosecond Ti:sapphire laser (Coherent, Mira), whose Synchro-Lock accessory phase-locked the seed pulses to a sub-harmonic of the radio frequency (RF) that drives the synchrotron ring. The Ti:sapphire laser was pumped by the frequency-doubled output from a single frequency solid-state Nd:YVO_4 laser (Coherent, 5W Verdi). This solid-state laser system generates stable, ultrashort, phase-locked pulses that are tunable from 475–800 nm with energy as high as 120 μJ per pulse.

2.3. X-ray source

The synchrotron was operated in the so-called four-bunch mode where four equally spaced electron bunches circulate in the storage ring. When passing through a U17 in-vacuum undulator (1.6 m long, 17 mm magnetic period, and 6.6 mm gap), a 45-nC bunch of 6-GeV electrons generates about 10^{10} X-ray photons with a wavelength peaked at 0.79 Å and a bandwidth of ~3.5% (FWHM). The duration of the X-ray pulse is a function of the charge in the electron bunch, with 35 nC producing a 150-ps long (FWHM) pulse. To isolate single pulses from the pulse train, the X-ray beam passes through a series of mechanical shutters, the fastest being a supersonic mechanical chopper (Wulff et al., 2003) whose opening time is shorter than the four-bunch mode inter-pulse separation of 704 ns. A toroidal mirror focuses the X-ray beam down to about 100 μm h × 60 μm v (FWHM). Slits then clean up the beam profile, collimating it to 120 μm h × 50 μm v.

2.4. Synchronization of X-ray and laser pulses

The synchrotron "bunch" clock provides a single-bunch timing signal that is synchronous with the 352 MHz RF that drives the accelerator cavities in the storage ring. The arrival of an X-ray pulse occurs at a constant delay relative to this clock. As the four-bunch ring current decays during its 6-h lifetime, the delay shifts somewhat, so this timing signal is precise to only about 50 ps. The Synchro-Lock electronics phase lock the mode-locked titanium-sapphire oscillator (Coherent Mira) to a sub-harmonic (88 MHz) of the synchrotron RF with timing jitter less than 5 ps (Naylor et al., 2001). The delay between the laser and X-ray pulses is measured at the sample with a high-speed gallium arsenide photoconductor (CEA, Bruyeres Le Chatel, France) that is responsive to both visible light and X-rays. The photoconductor signal is recorded with a 3-GHz oscilloscope (Tektronix, TDS-694; 10 GS/s sampling rate) whose ~120 ps rise time allows the delay between time-separated laser and X-ray pulses to be measured to a precision better than 50 ps. A digital delay generator (Stanford Research Systems, DG535) controls the injection of seed pulses into the regenerative amplifier, thereby changing the time delay in discrete steps of 11.4 ns ($88\,MHz^{-1}$). Fine timing over a 12-ns range is accomplished with 50 ps precision by shifting the phase of the RF signal to which the laser oscillator is locked. With this combination of timing control, the delay between laser and X-ray pulses can be set from 0 to 80 ms with a precision of 50 ps.

2.5. Laser photolysis

When the number of photons in a visible photolysis pulse is comparable to the number of chromophores within the illuminated volume of a P6 MbCO crystal, the peak power of a 100 fs pulse exceeds $10^{10}\,W/mm^2$. At these power levels, nonlinear absorption can take place and the sample can suffer photochemical damage. To minimize these problems, the photolysis pulse is stretched from 100 fs to ~100 ps using a combination of group velocity dispersion (GVD) and modal dispersion. The GVD through two 150-mm long Brewster-cut fused silica glass blocks stretches the pulse to the ps regime. This ps pulse is then launched into a 200-μm core size 3-m length of multimode optical fiber, whose modal dispersion further stretches the pulse to nearly 100 ps. Due to the high peak power of the laser pulse in the optical fiber, a nonlinear optical process shifts and broadens the 533 nm input pulse to a spectral range spanning 530–580 nm. This spectrally broadened pulse is delivered to the protein crystal through an optical assembly that images the output of the fiber onto the sample (Fig. 2). A cylindrical lens positioned near the fiber exit allows the focal spot to be tuned from circular to elliptical with the magnification set to maintain the minor dimension at 120 μm. The long axis of the elliptical spot is set parallel to the direction of the X-ray beam to maximize spatial overlap between the laser and X-ray pulses. To handle the broadband radiation with minimal chromatic aberration, the condenser optics are fashioned from two achromatic doublets and a meniscus lens. This fiber-based approach was adopted to achieve uniform illumination of the protein crystal with the pulse energy confined to the volume probed by the X-ray pulse. This improvement allows us to illuminate the crystal with higher average power densities. Because the stretched optical pulse remains short compared to the X-ray pulse, the time-resolution is still dictated by the X-ray pulse duration.

The Raman-broadened spectrum spans the Q-band of MbCO and was used without further filtering. Because the optical density of the P6 MbCO crystal near the peak of the Q-band is approximately 1 through 70 μm, high average photolysis can be expected only near the edge of the crystal. Hence, it is crucial to center the 50 μm (V) X-ray beam at a depth of ~25 μm from the top edge of the crystal. The pencil-like shape of the P6

MbCO crystals helps to maintain the alignment over ±30°- rotation.

Laser photolysis heats the protein crystal and can lead to distillation of mother liquor away from the crystal to cooler regions of the glass capillary. To reduce the rate of distillation during laser photolysis, the capillary was cooled in a N_2 gas stream set to 10 °C (Cryostream, Oxford Cryosystems).

2.6. Data collection

Laue diffraction data were acquired using unfiltered polychromatic X-ray pulses from the U17 undulator. By not filtering the radiation through a monochromator, the collection of time-resolved diffraction data is sped up enormously. The crystal scatters about 2×10^6 photons per X-ray pulse in the form of Bragg re-

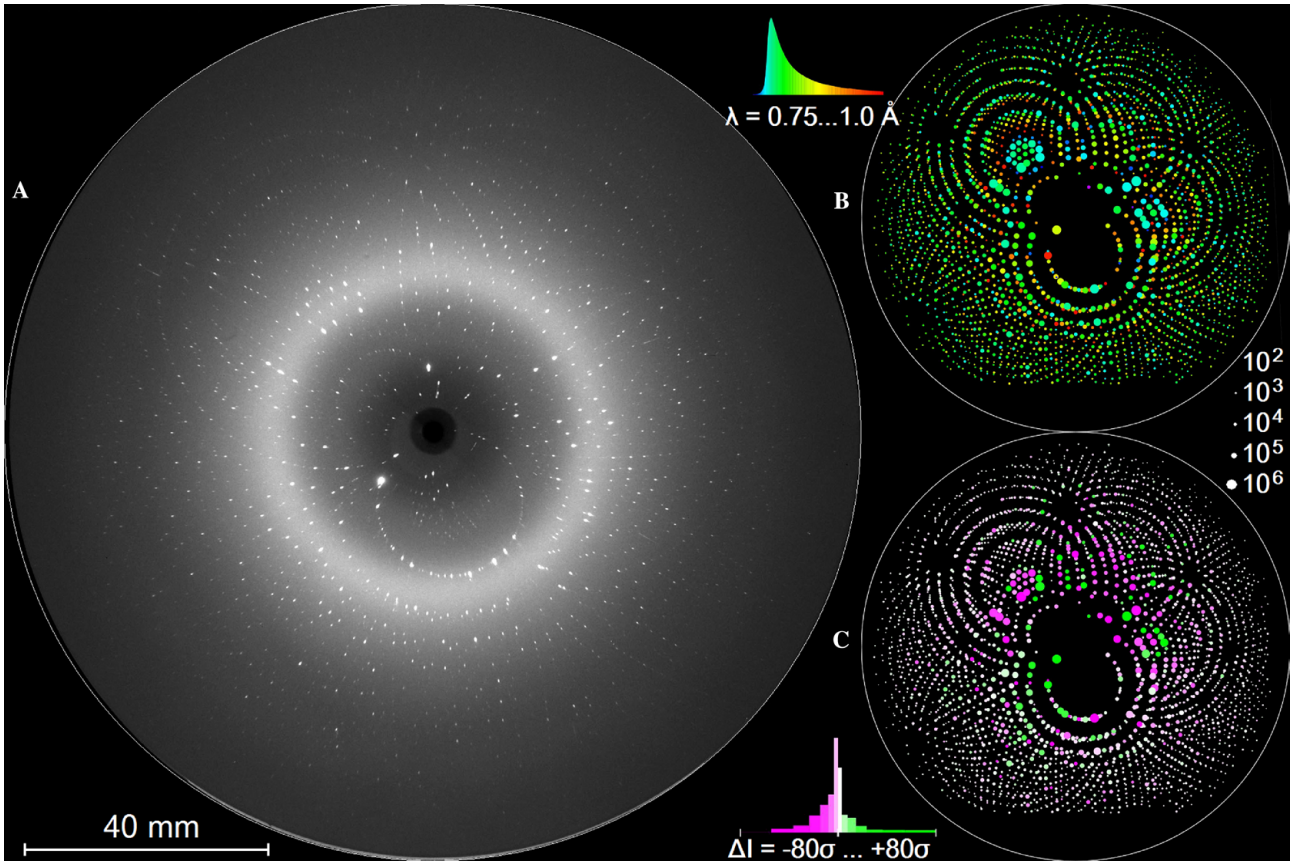

Fig. 3. (A) Time-resolved Laue diffraction image of a myoglobin crystal acquired 100 ps after photolysis with a CCD detector (2048 × 2048 pixels). The image represents the accumulation of 32 X-ray pulses over a 10 s period and contains about 3000 usable diffraction spots (B) Reflections color-coded by X-ray wavelength. The X-ray spectrum ranges from 0.75 to 1.0 Å and is peaked at 0.79 Å. The dot size indicates the number of photons in the diffraction spot. The strongest spots contain about 7×10^5 photons, with the sum of all spots totaling about 7×10^7 photons. (C) Photolysis-induced intensities changes. The reflections are color-coded according to the direction of change ΔI (green-positive; magenta-negative). The color saturation indicates their statistical significance (ΔI is the photolysis-induced change of the photon count; σ is the uncertainty of that change). Only 5.5% of the reflections change by more that 3σ (saturated green and magenta). However, this fraction contains 43% of all diffracted photons.

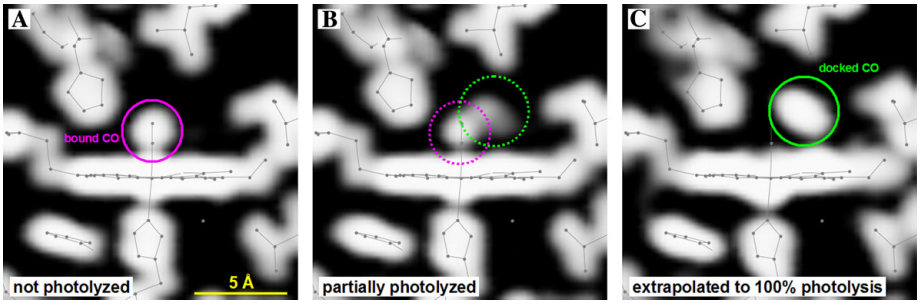

Fig. 4. (A) Electron density map of MbCO before photolysis. (B) Electron density of MbCO after about 25% photolysis (at 100 ps). Note the partial occupancy of CO in both binding and primary docking sites. (C) Electron density of the photolyzed state obtained after extrapolating the data from the middle image to complete photolysis.

Table 1
Data collection statistics

Data set	L29F 100 ps–3 ns	L29F 3.16 ns–3.16 μs	WT 100 ps–10 μs
Date	14 Apr 2002	15 Oct 2002	15 Dec 2003
Sample size	$200 \times 200 \times 200$ μm	$270 \times 280 \times 280$ μm	$720 \times 240 \times 240$ μm
Temperature	283 K	288 K	283 K
Pump wavelength	580 nm	580 nm	530–580 nm
Pump pulse length	~1 ps	2 ns	~100 ps
Pump energy	23 μJ	1.0 mJ	41 μJ
Pump focus	0.2×0.13 mm^2 FWHM	0.79 mm^2	0.24×0.11 mm^2 FWHM
Energy density	0.88 mJ/mm^2	0.79 mJ/mm^2	1.5 mJ/mm^2
Photolysis degree	20%	17%	25%
Pulses per image	32 (3.3 Hz)	16 (1 Hz)	16 (3.3 Hz)
Number of images	155	155	403
Collection time	1 h 15 min	2 h 27 min	1 h 49 min
Resolution (50% $I/\sigma > 3$)	2.0 Å	1.9 Å	2.1 Å
Observations	94 441	120 267	94 115
Redundancy	4.8	5.2	4.9
R_{sym}	0.21	0.12	0.18
$\langle I/\sigma \rangle$	7.3	9.9	7.1
	All	$I/\sigma > 3$	All	$I/\sigma > 3$	All	$I/\sigma > 3$
Unique reflections (Å)						
30.0–6.0	498	487	529	523	491	475
6.0–2.9	4273	4004	4234	4104	4204	3863
2.9–2.4	3626	3067	3585	3241	3567	2825
2.4–2.0	6032	4095	5993	4778	5931	3540
2.0–1.9	2356	983	2365	1457	2312	824
1.9–1.8	2877	723	2959	1419	2730	590
1.8–1.7	—	—	3526	1151	—	—
Overall	19 658	13 355	23 191	16 670	19 231	12 113
Completeness (Å)						
30.0–6.0	0.80	0.78	0.84	0.83	0.84	0.81
6.0–2.9	0.92	0.86	0.91	0.89	0.91	0.83
2.9–2.4	0.94	0.79	0.93	0.84	0.92	0.73
2.4–2.0	0.94	0.64	0.93	0.74	0.92	0.55
2.0–1.9	0.94	0.39	0.94	0.58	0.92	0.33
1.9–1.8	0.91	0.23	0.94	0.45	0.87	0.19
1.8–1.7	—	—	0.92	0.30	—	—
Overall	0.93	0.63	0.93	0.73	0.91	0.57

flections, which are recorded on an area detector (MAR CCD, MAR Research). The detector has an X-ray scintillator of 132.5 mm diameter, whose light output is coupled through a tapered fiber optic bundle to a 2048×2048 pixels CCD. To improve the signal-to-noise ratio of the diffraction images, 16 or 32 pulses with the same photolysis-probe delay are accumulated on the detector at a rate of 3.3 Hz before being read. Each diffraction image (Fig. 3A) contains about 3000 Bragg reflections, the strongest containing about 700 000 photons and the weakest usable ones containing fewer than 100 photons (Fig. 3B). A single image measures about 15% of the structure factors required to calculate a three-dimensional electron density map. To acquire a complete data set, we record images at 31 different orientations of the crystal, which provide about 100 000 observations of 20 000 unique structure factors. The aim of the experiment is to measure photolysis-induced structure changes as a function of time. To minimize systematic error in the time-resolved structures due to sample degradation, the entire time series is acquired before advancing the goniometer spindle to a new crystal orientation. The first image in each time series is recorded without firing the laser, and is used to build a reference data set for the unphotolyzed structure. Statistics for the data sets are summarized in Table 1. Although only a small fraction of the detected intensity changes are statistically significant (Fig. 3C), the fact that we measure so many of them, and because all structure factors, through Fourier transformation, contribute to the electron density at each point in real space, we obtain statistically significant electron density changes in the maps.

2.7. Data analysis

The following software was used: LAUEGEN (Campbell, 1995) for indexing, PROW (Bourgeois et al., 2000) for integration, LSCALE (Arzt, 1999) for

wavelength normalization, and CCP4 (Daresbury Laboratory, UK) for scaling and electron density map generation.

We generated σ_A-weighted $2F_o$–F_c maps of the unphotolyzed and photolyzed states (Figs. 4A and B) with phases calculated from the model of the unphotolyzed state. Calculated structure factors and phases were obtained from models of wild-type and L29F MbCO (PDB coordinate files 2MGK and 2SPL).

2.8. Extrapolation to full photolysis

Because the sample is only partially photolyzed, the $2F_o$–F_c map (Fig. 4B) represents a mixture of the photolyzed and unphotolyzed state. To obtain maps of the photolyzed state, which are more readily interpreted, we extrapolated the electron density to complete photolysis according to the formula

$$\rho_o = \rho_{\text{off}} + (1/x) \cdot (\rho_{\text{on}} - \rho_{\text{off}}).$$

ρ_{off} and ρ_{on} are the experimentally determined unphotolyzed and partially photolyzed electron densities and x is the photolysis degree, which was estimated by finding the value where bound CO vanishes from the extrapolated map. The degree of photolysis was typically found to be around 20–25%. The fully photolyzed state, calculated according to this procedure is shown in Fig. 4C.

2.9. Novel rendering of electron density maps

Although the dissociation of CO is clearly visible in the extrapolated map (Fig. 4C), more subtle photolysis-induced changes such as conformational relaxation of the protein are not easily discerned. Traditionally, small changes in electron density are presented by generating a difference map and rendering negative and positive difference densities as iso-surfaces in two different colors (Fig. 5A). The drawback of this method is that only electron density above the threshold of the chosen contouring level is visible. To reveal more subtle features, the threshold would need to be lowered, but then the weak features would dominate the image and make it very cluttered. An improved way to render the electron difference density is by mapping density to brightness, as shown in Fig. 5B. With this approach, each volume element is assigned a color based on the sign and a brightness based the absolute value of the density difference. Projecting the color-coded voxels onto a plane produces maps whose varying shades of color correlate with varying electron density. To show weak features in the presence of strong features, the density difference is mapped to color brightness nonlinearly, which is analogous to the gamma correction employed in image editing. The nonlinear function used here, however, increases monotonically with electron density and asymptotically approaches saturation. For small density differences, the resulting color shade has a brightness that is proportional to the difference. The asymptotic approach to saturation compresses the dynamic range of the image, thereby ensuring that the color shade for large differences remains below saturation.

In difference maps, the difference features are not centered on the group of atoms that are moving (except when they move atomic distances, such as CO translocation), but are localized near their edges. When matching pairs of positive and negative density can be assigned to an atom, the direction of motion is from the negative (magenta) density to the positive (green) density. However, matching pairs are often separated by large gaps, making the assignment of difference features to atoms somewhat ambiguous.

The problem of visualizing structural changes in proteins is a general one, and the need for improved tools is self evident, especially in the area of time-resolved crystallography. Therefore, we sought to develop an improved method for rendering electron density maps so that they can be visually interpreted intuitively. Here, we introduce a new method of image rendering (Fig. 5C) in which color-coded maps of the unphotolyzed and photolyzed structures are superimposed. The electron density of the unphotolyzed state is colored magenta and that of the photolyzed state is green. The saturation of the blended color is determined by the ratio of the two densities, and varies continuously from magenta to grey to green. White and shades of grey indicate no change in electron density. Nonlinear mapping of density to brightness is accomplished by relating the brightness of the blended color to electron density in a fashion that preserves the saturation (ratio) of the blended colors. The magenta to green color gradient indicates the direction of motion, and the width of the colored fringes on both sides of the grey band correlate with the amplitude of the motion. Since the electron density is centered on the atoms that give rise to that density, there is no ambiguity in the assignment. Nonlinear mapping of the electron density to color brightness highlights weak features, such as migrating ligands, that might otherwise get lost in the background. In Fig. 5C, the correlated motion of the heme, CO, and surrounding residues is intuitively presented by the magenta to green color gradients, as annotated with yellow arrows.

The details and the code for rendering images in this fashion will be published separately.

2.10. Results and discussion

The time-resolved structure differences depicted in Fig. 6 reveal correlated displacements spanning the entire protein in both wild-type and mutant Mb. Except for the residues near the mutated 29 position, the displacements in wild-type and mutant Mb are remarkably

similar, suggesting a common origin for this motion. The driving force for these global structure changes resides in the photolysis-induced doming of the heme. For stereochemical reasons, when the Fe atom of the heme loses one of its six binding partners, the geometry of the heme changes from planar to domed, with the Fe atom moving 0.3 Å (Kachalova et al., 1999) or 0.36 Å (Vojtechovsky et al., 1999) out of the heme plane. This displacement is transmitted through His93 on the proximal side of the heme to the F helix. However, the proximal response only partially accommodates the forces generated by heme doming: the porphyrin ring of the heme is pushed upward, dragging with it residues Leu104 and Ile107 and the G helix to which they are attached. The heme motion appears to be hinge-like, with its propionate side chains serving as the hinge point. According to X-ray models, the heme propionates are tethered to the surface of the protein through hydrogen bonds with Arg45 and His97, and that tether may provide a lever advantage that magnifies the displacement of the G helix.

The global conformational changes propagate from the heme throughout the entire protein within our experimental time resolution of 150 ps. If this motion were an elastic protein response to heme doming, it could propagate as fast as the speed of sound. Indeed, results from fs time-resolved transient phase grating spectroscopy suggest that after photolysis, Mb expands along the direction perpendicular to the heme plane within 500 fs (Goodno et al., 1999). To follow this ultrafast process with X-ray crystallography would require a 4th generation X-ray source, such as the proposed LCLS at Stanford (Cho, 2002) or TESLA-FEL in Hamburg (Abd-Elmeguid et al., 2001). Until such a source becomes available, we can observe only the over-damped conformational relaxation that is triggered by the photolysis-induced protein quake (Ansari et al., 1985).

The most significant structural differences between wild-type and mutant Mb are confined to the vicinity of the binding site. When wild-type MbCO is photolyzed, CO appears promptly in the primary docking site, Leu29 is displaced upward, and His64 moves to occupy

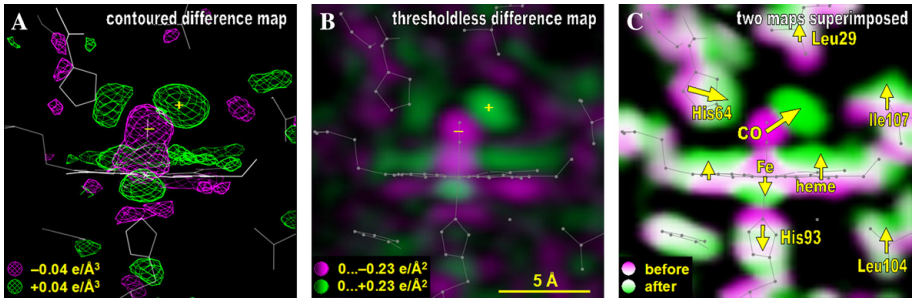

Fig. 5. (A) Contoured difference map corresponding to the photolysis-induced structure changes occurring in MbCO at 100 ps (green-positive; magenta-negative). (B) Thresholdless difference map of the same data. The electron density was mapped nonlinearly to color brightness. (C) Color-coded superposition of electron density maps recorded for the ground state (magenta) and photolyzed state (green). The electron density of the photolyzed state was estimated by extrapolating the measured electron density to 100% photolysis. The electron density was mapped nonlinearly to color brightness. Where magenta and green overlap, they blend to white. The direction of motion, as indicated by the arrows, follows the magenta-to-green color gradient.

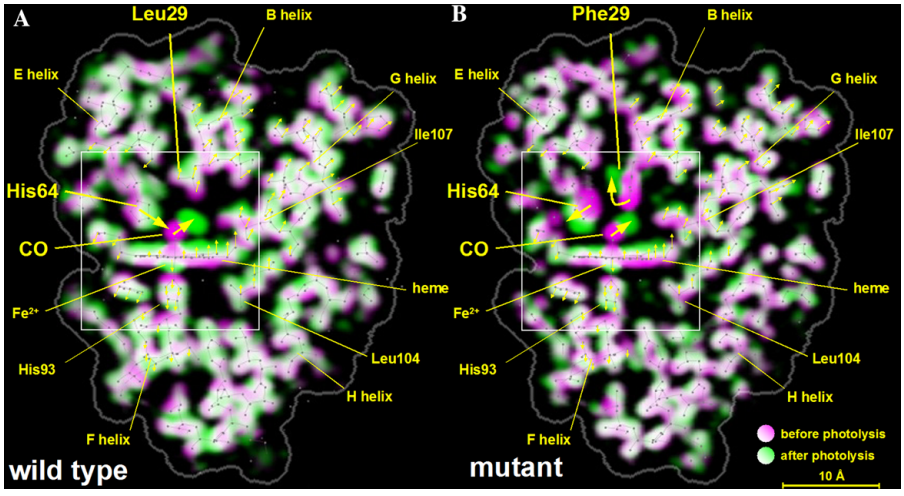

Fig. 6. Structural changes in wild-type (A) and mutant (B) MbCO determined 100 ps after photolysis. The most dramatic changes occur within the area enclosed by the white box, but smaller changes are evident over the entire dimensions of the protein.

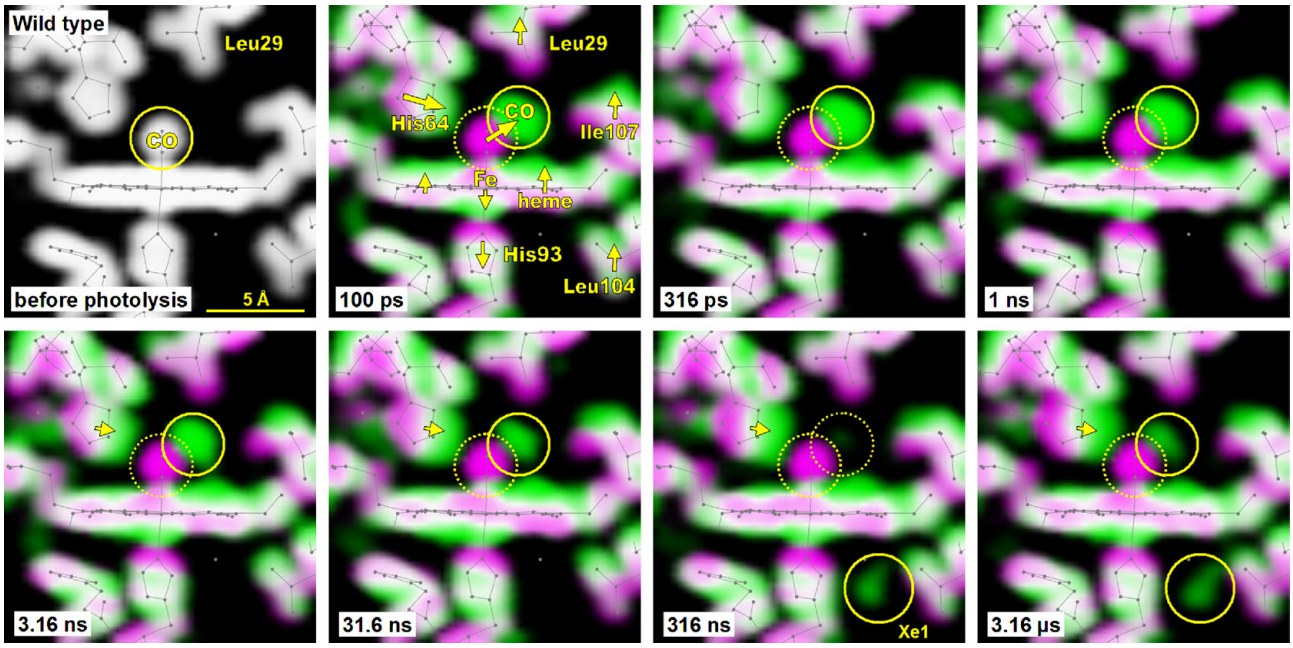

Fig. 7. Time dependence of CO migration and structural relaxation in wild-type MbCO. The solid circles denote occupied CO sites and the dotted circles denote evacuated CO sites. The photolyzed CO is initially trapped in the primary docking site about 2 Å from the binding site and subsequently migrates to the Xe1 site on the opposite side of the heme. The stick model represents the unphotolyzed structure, which provides a static reference frame for the time-resolved electron density changes. Note the prompt movement of His64 toward the binding site in the 100 ps map. As CO escapes from the primary docking site, the color contrast across His64 increases, indicating further relaxation of that side chain. (See Movies 2 and 4 in supplemental online information.)

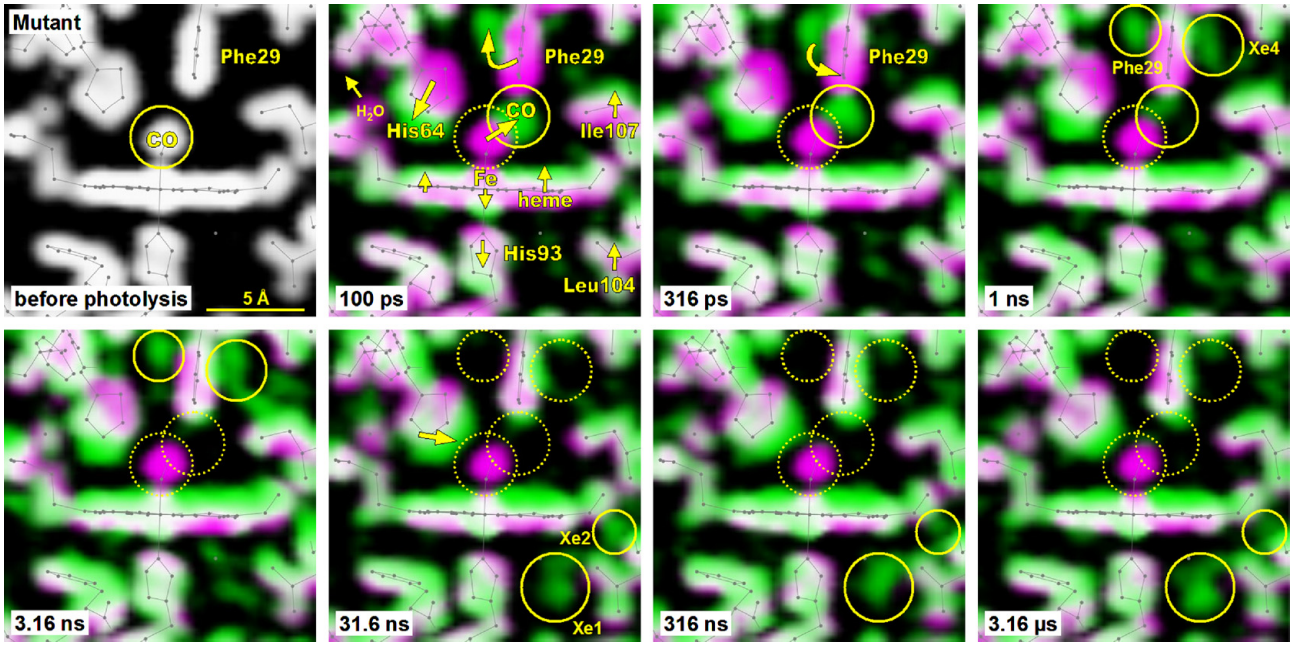

Fig. 8. Time dependence of CO migration and structural relaxation in mutant MbCO. Initially, CO is trapped in the primary docking site, which is similar to that of wild-type Mb. Its presence displaces the side chains of Phe29 and His64, whose strain helps expedite the departure of CO out of this site. It escapes to the sites labeled Phe29 and Xe4 with approximately equal probability. The CO continues its migration with a portion of the CO density reappearing on the opposite side of the heme, where it accumulates in the sites Xe1 and possibly Xe2. Note that His64 initially moves away from the binding site, but later relaxes toward the binding site. The most dramatic differences in the side chain motion of wild-type and L29F Mb are manifested in the sub-ns maps, demonstrating the need to probe protein dynamics on a sub-ns time scale. (See Movies 1 and 3 in supplemental online information.)

the void left behind by the CO. In the mutant, CO appears in the same docking site, but the displacement of Phe29 is far more dramatic than that observed for Leu29 in wild-type. The Phe29 collides with His64, pushing it in a direction nearly opposite that observed in wild-type. The large-scale excursion of the Phe29 can be explained by the fact that its benzene ring significantly reduces the volume available for the CO in the heme pocket docking site, so the only way CO can be accommodated in that site is by pushing aside both Phe29 and His64.

As shown in Figs. 7 and 8, the structural differences for wild-type and mutant Mb continue to evolve over time. In wild-type Mb (Fig. 7), CO persists in the primary docking site for a few hundred ns, after which it escapes and then accumulates in the Xe1 site on the opposite side of the heme plane. The Xe1 site is one of four internal cavities that trap xenon under pressure (Tilton et al., 1984). Their occupancy decreases from Xe1 to Xe4, likely reflecting the relative size of those cavities. In the L29F mutant (Fig. 8), CO escapes from the primary docking site within 1 ns, and then accumulates in two sites: one is the equivalent of Xe4; the other is a small cavity on the opposite side of Phe29. Evidently, the strain induced on Phe29 by the transiently trapped CO is relieved when CO pops up on either side of the aromatic ring. These two states are short-lived, with CO departing within about 10 ns and then accumulating primarily in the Xe1 site, though there is a hint that Xe2 becomes partially occupied as well. We see a hint of CO accumulating in the Xe4 site of wild-type Mb, suggesting that CO may pass through Xe4 en route to Xe1. Because the lifetime of CO in Xe4 (as measured in the L29F mutant) is short compared to the lifetime of CO in the primary docking site, the maximum Xe4 occupancy is relatively low.

In the last two frames of the wild-type MbCO time series, electron density in the primary docking site grows substantially. We believe this growth arises from water diffusing to this site. We know from equilibrium structures of wild-type deoxy Mb that this site is partially occupied (0.84) by a water molecule that is hydrogen bonded to His64 (Quillin et al., 1993). Our work suggests that water accesses the docking site with a rate of approximately $(1\,\mu s)^{-1}$. The fact that the electron density in this site goes through a minimum before growing again suggests that the rate of water entry is slow compared to the rate at which CO escapes from the primary docking site. Because the primary docking site has insufficient volume to accommodate both molecules, CO must depart before water can enter. Note that the rate of water entry is somewhat slower than the rate at which water binds to met Mb in solution, which was found to be about $(175\,ns^{-1})$ (Cao et al., 2001). The rate of water entry into a protein that is confined in a crystal might be expected to be slower than the rate when the protein is free in solution, e.g., crystal packing forces may constrain conformational fluctuations that open and close channels through which water (or other ligands) can pass. In contrast to wild-type Mb, there is no re-growth of electron density in the primary docking site of L29F Mb. This observation is consistent with the fact that no water is found in the crystal structure of deoxy L29F Mb (PDB file: 1MOA). Evidently, steric hindrance by the Phe29 sidechain excludes water from the primary docking site.

The correlated CO and protein side chain motion in wild-type and L29F Mb differ dramatically on the picosecond time scale, illustrating how a modest mutation can alter the mechanism by which a toxic ligand is excreted. Spectroscopic measurements have shown that geminate CO rebinding is modest in wild-type Mb (Henry et al., 1983), but it is nearly absent in L29F Mb (Schotte et al., 2003). In wild-type Mb, His64 promptly moves toward the binding site and raises a steric barrier to geminate rebinding. Because the CO residence time in the primary docking site is a few hundred nanoseconds, the barrier height must be sufficiently high to keep geminate rebinding to a minimum. In the L29F mutant, the added steric encumbrance in the vicinity of the primary docking site leads to strain that is relieved when CO is rapidly swept away from the primary docking site. After CO departs, His64 relaxes to a position similar to that found in wild-type Mb.

We cannot observe the actual diffusion of CO inside the protein because ligand translocation between internal cavities is not only too fast to be resolved, but is not synchronized among the 10^{13} or so proteins probed by the X-ray pulse. With time-resolved crystallography, we see only sites where a measurable fraction of CO has accumulated at that point in time. The CO likely migrates between internal cavities in a hopping fashion, and spends most of its time rattling around within an internal cavity while awaiting a protein fluctuation that opens a channel through which it can pass to another cavity. Consequently, time-resolved X-ray crystallography is sensitive to intermediates whose population is sufficient to be observed.

That CO migrates to the Xe1 site was shown indirectly through mutagenesis and Xe studies (Scott et al., 2001) as well as directly through cryo-crystallography (Chu et al., 2000; Ostermann et al., 2000) and nanosecond time-resolved crystallography (Bourgeois et al., 2003; Srajer et al., 2001). Cryo-crystallographic studies of the L29W mutant of Mb, which is similar to the L29F mutant reported here, also found CO trapped in the Xe4 site (Ostermann et al., 2000). When their crystal was illuminated above 180 K and then quickly cooled to 105 K for data collection, the CO was found in the Xe1 site. Moreover, they found the backbone displacements to be much larger, illustrating how protein motions are inhibited below the glass transition temperature. That

study helps to expose the connectivity of internal cavities through which ligands can pass prior to finding an escape pathway to the surrounding solvent. By recording time-resolved structures under ambient conditions, we are able to see not only the correlated motion of the protein that accompanies ligand migration, but also characterize the time regime over which such motions occur. These experimental measurements necessarily involve an ensemble of molecules, each of which marches to the beat of its own drum. To unravel the ensemble average, we have performed a joint analysis of time-resolved X-ray structures and MD simulations. That study, which will be published elsewhere, shows how cross-validated experimental and computational results can help elucidate a mechanistic understanding of protein function at the single molecule level (Hummer et al., 2004).

Acknowledgments

We thank the ESRF for their generous allocation of beamtime over the past six years, and the staff of the ID09 beamline, Maciej Lorenz, Laurent Eybert, and Anton Plech, for their assistance. We thank W. Eaton, G. Hummer, and Fred Dyda for helpful comments, and D. Bourgeois for sharing his expertise in the analysis of Laue diffraction data. We are grateful to K. Moffat and V. Šrajer for their assistance and encouragement as we sought to extend time-resolved X-ray crystallography to the picosecond time domain. This work was supported by grants from the Robert A. Welch Foundation (C-612), the NIH (HL47020 and GM35649), and the W. M. Keck Center for Computational Biology to J.O.

Appendix. Supplementary material

Supplementary data associated with this article can be found, in the online version, at doi:10.1016/j.jsb.2004.06.009.

References

Abd-Elmeguid, M., et al., Materlik, G., Tschentscher, T. (Eds.), In: TESLA: The Superconducting Electron-Positron Linear Collider with Integrated X-ray Laser Laboratory—Technical Design Report (DESY, Hamburg, 2001), vol. V, p. 333.

Ansari, A., Berendzen, J., Bowne, S.F., Frauenfelder, H., Iben, I.E., Sauke, T.B., Shyamsunder, E., Young, R.D., 1985. Protein states and proteinquakes. Proc. Natl. Acad. Sci. USA 82, 5000–5004.

Arzt, S., 1999. LSCALE—the new normalization, scaling and absorption correction program in the Daresbury Laue software suite. J. Appl. Cryst. 33, 554–562.

Austin, R.H., Beeson, K.W., Eisenstein, L., Frauenfelder, H., Gunsalus, I.C., 1975. Dynamics of ligand binding to myoglobin. Biochemistry 14, 5355–5373.

Bourgeois, D., Vallone, B., Schotte, F., Arcovito, A., Miele, A.E., Sciara, G., Wulff, M., Anfinrud, P., Brunori, M., 2003. Complex landscape of protein structural dynamics unveiled by nanosecond Laue crystallography. Proc. Natl. Acad. Sci. USA 100, 8704–8709.

Bourgeois, D., Wagner, U., Wulff, M., 2000. Towards automated Laue data processing: application to the choice of optimal X-ray spectrum. Acta Cryst. D, 973–985.

Brooks III, C.L., Karplus, M., Pettitt, B.M., 1988. Proteins: a theoretical perspective of dynamics, structure and thermodynamics Advances in Chemical Physics, vol. 71. Wiley, New York.

Brunori, M., Bourgeois, D., Vallone, B., 2004. The structural dynamics of myoglobin. J. Struct. Biol. 147, 223–234.

Brunori, M., Vallone, B., Cutruzzola, F., Travaglini-Allocatelli, C., Berendzen, J., Chu, K., Sweet, R.M., Schlichting, I., 2000. The role of cavities in protein dynamics: crystal structure of a photolytic intermediate of a mutant myoglobin. Proc. Natl. Acad. Sci. USA 97, 2058–2063.

Campbell, J.W., 1995. LAUEGEN, an X-windows-based program for the processing of Laue X-ray diffraction data. J. Appl. Cryst 18, 228–236.

Cao, W., Christian, J.F., Champion, P.M., Rosca, F., Sage, J.T., 2001. Water penetration and binding to ferric myoglobin. Biochemistry 40, 5728–5737.

Carlson, M.L., Regan, R., Elber, R., Li, H., Phillips Jr., G.N., Olson, J.S., Gibson, Q.H., 1994. Nitric oxide recombination to double mutants of myoglobin: role of ligand diffusion in a fluctuating heme pocket. Biochemistry 33, 10597–10606.

Carver, T.E., Brantley Jr., R.E., Singleton, E.W., Arduini, R.M., Quillin, M.L., Phillips Jr., G.N., Olson, J.S., 1992. A novel site-directed mutant of myoglobin with an unusually high O_2 affinity and low autooxidation rate. J. Biol. Chem. 267, 14443–14450.

Cho, A., 2002. Physics. The ultimate bright idea. Science 296, 1008–1010.

Chu, K., Vojtchovsky, J., McMahon, B.H., Sweet, R.M., Berendzen, J., Schlichting, I., 2000. Structure of a ligand-binding intermediate in wild-type carbonmonoxy myoglobin. Nature 403, 921–923.

Elber, R., Karplus, M., 1990. Enhanced sampling in molecular dynamics: use of the time-dependent Hartree approximation for a simulation of carbon monoxide diffusion through myoglobin. J. Am. Chem. Soc. 112, 9161–9175.

Gibson, Q.H., Ainsworth, S., 1957. Photosensitivity of haem compounds. Nature 180, 1416–1417.

Gibson, Q.H., Regan, R., Elber, R., Olson, J.S., Carver, T.E., 1992. Distal pocket residues affect picosecond ligand recombination in myoglobin. An experimental and molecular dynamics study of position 29 mutants. J. Biol. Chem. 267, 22022–22034.

Goodno, G.D., Astinov, A., Miller, R.J.D., 1999. Femtosecond Heterodyne-Detected Four-Wave-Mixing Studies of Deterministic Protein Motions. 2. Protein Response. J. Phys. Chem. A 103, 10630–10643.

Henry, E.R., Sommer, J.H., Hofrichter, J., Eaton, W.A., 1983. Geminate recombination of carbon monoxide to myoglobin. J. Mol. Biol. 166, 443–451.

Hummer, G., Schotte, F., Anfinrud, P.A., 2004. Unveiling functional protein motions with picosecond x-ray crystallography and molecular simulations. (in preparation).

Kachalova, G.S., Popov, A.N., Bartunik, H.D., 1999. A steric mechanism for inhibition of CO binding to heme proteins. Science 284, 473–476.

Lim, M.H., Jackson, T.A., Anfinrud, P.A., 1995. Midinfrared vibrational-spectrum of CO after photodissociation from heme evidence for a ligand docking site in the heme pocket of hemoglobin and myoglobin. J. Chem. Phys. 102, 4355–4366.

McCammon, J.A., Harvey, S.C., 1987. Dynamics of Proteins and Nucleic Acids. Cambridge University Press, New York.

Moffat, K., 2001. Time-resolved biochemical crystallography: a mechanistic perspective. Chem. Rev. 101, 1569–1581.

Naylor, G.A., Scheidt, K., Larsson, J., Wulff, M., Filhol, J.M., 2001. A sub-picosecond accumulating streak camera for X-rays. Meas. Sci. Technol. 12, 1858–1864.

Olson, J.S., Phillips Jr., G.N., 1996. Kinetic pathways and barriers for ligand binding to myoglobin. J. Biol. Chem. 271, 17596.

Ostermann, A., Waschipky, R., Parak, F.G., Nienhaus, G.U., 2000. Ligand binding and conformational motions in myoglobin. Nature 404, 205–208.

Phillips Jr., G.N., Arduini, R.M., Springer, B.A., Sligar, S.G., 1990. Crystal structure of myoglobin from a synthetic gene. Proteins 7, 358–365.

Quillin, M.L., Arduini, R.M., Olson, J.S., Phillips Jr., G.N., 1993. High-resolution crystal structures of distal histidine mutants of sperm whale myoglobin. J. Mol. Biol. 234, 140–155.

Quillin, M.L. et al., 1995. Structural and functional effects of apolar mutations of the distal valine in myoglobin. J. Mol. Biol. 245, 416–436.

Sassaroli, M., Rousseau, D.L., 1986. Simulation of carboxymyoglobin photodissociation. J. Biol. Chem. 261, 16292–16294.

Schlichting, I., Berendzen, J., Phillips Jr., G.N., Sweet, R.M., 1994. Crystal structure of photolysed carbonmonoxy-myoglobin. Nature 371, 808–812.

Schlichting, I., Chu, K., 2000. Trapping intermediates in the crystal: ligand binding to myoglobin. Curr. Opin. Struct. Biol. 10, 744–752.

Schotte, F., Lim, M., Jackson, T.A., Smirnov, A.V., Soman, J., Olson, J.S., Phillips Jr., G.N., Wulff, M., Anfinrud, P.A., 2003. Watching a protein as it functions with150-ps time-resolved X-ray crystallography. Science 300, 1944–1947.

Scott, E.E., Gibson, Q.H., Olson, J.S., 2001. Mapping the pathways for O_2 entry into and exit from myoglobin. J. Biol. Chem. 276, 5177–5188.

Srajer, V. et al., 2001. Protein conformational relaxation and ligand migration in myoglobin: a nanosecond to millisecond molecular movie from time-resolved Laue X-ray diffraction. Biochemistry 40, 13802–13815.

Srajer, V. et al., 1996. Photolysis of the carbon monoxide complex of myoglobin: nanosecond time-resolved crystallography. Science 274, 1726–1729.

Teng, T.Y., Srajer, V., Moffat, K., 1994. Photolysis-induced structural changes in single crystals of carbonmonoxy myoglobin at 40 K. Nat. Struct. Biol. 1, 701–705.

Tilton Jr., R.F., Kuntz Jr., I.D., Petsko, G.A., 1984. Cavities in proteins: structure of a metmyoglobin-xenon complex solved to 1.9 A. Biochemistry 23, 2849–2857.

Vitkup, D., Petsko, G.A., Karplus, M., 1997. A comparison between molecular dynamics and X-ray results for dissociated CO in myoglobin. Nat. Struct. Biol. 4, 202–208.

Vojtechovsky, J., Chu, K., Berendzen, J., Sweet, R.M., Schlichting, I., 1999. Crystal structures of myoglobin-ligand complexes at near-atomic resolution. Biophys. J. 77, 2153–2174.

Wulff, M., Plech, A., Eybert, L., Randler, R., Schotte, F., Anfinrud, P., 2003. The realization of sub-nanosecond pump and probe experiments at the ESRF. Faraday Discuss. 122, 13–26.

Ye, X., Demidov, A., Champion, P.M., 2002. Measurements of the photodissociation quantum yields of MbNO and MbO(2) and the vibrational relaxation of the six-coordinate heme species. J. Am. Chem. Soc. 124, 5914–5924.